

Tunable Multi-Peak Perfect Absorbers Based on Borophene for High-Performance Near-Infrared Refractive Index Sensing

Ruda Jian^{1 #}, Shiwen Wu^{1 #}, Bo Zhao², Guoping Xiong^{1,*}

¹Department of Mechanical Engineering, The University of Texas at Dallas, Richardson, TX 75080, United States.

²Department of Mechanical Engineering, University of Houston, Houston, TX 77004, United States.

These authors contribute equally to this work.

*Corresponding author. Email: Guoping.Xiong@UTDallas.edu

Abstract

Borophene has recently attracted significant attention as an emerging two-dimensional mono-elemental material for refractive index sensing because of its ultra-high surface-to-volume ratio and outstanding surface sensitivity. However, current research mainly focuses on designing borophene-based sensors with single-peak absorption, which lacks reliability compared to the performance of multi-peak sensors. In this paper, high-performance borophene refractive index sensors with multiple nearly perfect absorption peaks are proposed. The geometric parameters of the metadevices are optimized using finite-difference time-domain (FDTD) simulations to obtain three strong absorption peaks in the near-infrared (near-IR) regime with intensities of 99.72%, 99.18%, and 98.13%. Further calculations show that the sensitivities of the three strong peaks reach 339.1 nm shift per refractive index units (nm/RIU), 410.1 nm/RIU, and 738.1 nm/RIU, and their corresponding figure of merits (FOMs) reach up to 15.41/RIU, 14.65/RIU and 10.85/RIU, respectively, exhibiting great potential for near-IR refractive index sensing. Moreover, the three absorption peaks can be easily tuned by adjusting the carrier density of borophene, which can be realized by applying different external electric bias voltages. These results can provide theoretical guidance for the development of multi-peak near-IR dynamic integrated photonic devices.

Keywords Borophene · Multi-peak · Perfect absorption · Refractive index sensor

Introduction

As a new member of the two-dimensional (2D) monoelemental material (Xene) family, borophene has recently attracted tremendous attention because of its high thermal conductivity, excellent mechanical and electronic transport properties, and anisotropic optical behavior [1–4]. Similar to other 2D materials [5–8], borophene exhibits great potential for refractive index sensing because of its ultra-high surface-to-volume ratio and outstanding surface sensitivity [7–9]. In particular, borophene possesses a high carrier density ($\sim 10^{19} \text{ m}^{-2}$) [13,14], several orders of magnitude higher than those of other 2D materials such as graphene and black phosphorus ($\sim 10^{17} \text{ m}^{-2}$) [12,13], enabling borophene-based plasmonic devices to work in the visible and near-infrared (near-IR) regimes. In contrast to visible or near-IR sensors based on noble metals [17,18], the working wavelength of borophene devices can be easily tuned by applying external electric bias voltages to control its carrier density [19,20], making borophene-based sensors potentially suitable to operate in a broad wavelength range. Meanwhile, borophene devices possess unique advantages of 2D resonators such as high mode volume and strong light-confinement in the atomic scale [21], resulting in high detection sensitivity.

Although many refractive index sensors based on 2D materials have been widely reported, most of them are based on a single-peak absorption mechanism [9,22,23]. Compared to refractive index sensors relying only on single absorption peak, sensors with multiple absorption peaks can be used to monitor multiple modes of interest, and these multiple absorption peaks can generate more sensing information, thus reducing the error and improving the reliability of data [12,24,25]. For instance, refractive index sensors based on patterned graphene or gold layers exhibit three absorption peaks in the mid-IR regime [11,26] and can provide reliable sensing data associated

with multiple vibrational signatures of targeted molecules. To date, borophene refractive index sensors with multiple absorption peaks have not been reported.

In this letter, we propose a design of multi-peak borophene-based metadevices for efficient refractive index sensing applications. Our design can achieve three nearly perfect absorption peaks in the near-IR regime, resulting in excellent sensing performance that is comparable to or even better than that of the single-peak refractive index sensors in existing work. Moreover, these absorption peaks can be easily tuned by changing the carrier density of borophene, making the proposed borophene sensors highly promising for operations within a broad wavelength range.

Structure and Computational Method

The schematic diagrams of the borophene devices are shown in Figs. 1a-b. Fig. 1a displays the global view of a unit cell in a typical metadvice, in which a borophene grating layer lies on a dielectric layer with a refractive index of 1.4, and a gold film is employed as a reflective layer placed at the bottom of the absorber. Here, the thickness of borophene $d_B = 0.3$ nm is adopted to simulate the borophene monolayer [9,27]. The thicknesses of the dielectric layer d_1 and gold film d_2 are set to be 150 nm and 100 nm, respectively. As shown in the top view of a unit cell in the metadvice (Fig. 1b), the patterned borophene layer comprises of two symmetrical nano-ribbons and a nano-rectangle. p represents a single period of the unit cell. l and w represent the length and width of the nano-ribbons, respectively. g and h represent the x span and y span of the nano-rectangle, respectively. s and m represent the distance between the nano-ribbon and the nano-rectangle along y direction and the distance between the nano-rectangle to the edge along the x direction, respectively. j and k represent the distance between the nano-ribbons and the edge along the x direction and y direction, respectively. The distances (denoted as s) between the nano-rectangle and both nano-ribbons are kept the same.

The interactions between incident light and borophene metadevices are simulated by commercial finite-difference time-domain (FDTD) software (Lumerical 2021 R2.2) with a three-dimensional model constructed in the FDTD solver. Periodic boundary conditions are employed in both x and y directions to mimic the periodic structure of the borophene pattern, and perfect matching layer (PML) boundary condition is employed in the z direction. Two power monitors are placed $2 \mu\text{m}$ above and under the borophene metadvice to collect the reflectivity (R) and transmissivity (T), respectively. The absorptivity (A) spectrum can thus be calculated from the corresponding reflectivity and transmissivity spectra as $A = 1 - R - T$. Note that T is zero since the structure is opaque (Supplementary Fig. S1). In all simulations, mesh sizes of 1 nm in the x and y directions, and 0.15 nm in the z direction are used. Optical parameters of gold are taken from Ref. [28]. A Drude model is employed to calculate the anisotropic optical conductivity of borophene [29]:

$$\sigma_{jj}(\omega) = \frac{iD_j}{\pi(\omega + i\tau^{-1})}, D_j = \frac{\pi e^2 n_s}{m_j} \quad (1)$$

where j indicates the direction of optical axes of borophene crystal and can be chosen as x or y . ω is the angular frequency of light, and τ is the electron relaxation time and set as 65 fs . D_j represents the Drude weight, where e is the electron charge, and n_s is the carrier density and is initially set as $4.3 \times 10^{19} \text{ m}^{-2}$. m_j is the effective electron mass in two crystal axis directions. Here, $m_x = 1.4 m_0$ and $m_y = 5.2 m_0$, where m_0 represents the rest mass of electrons. The effective permittivity of the borophene monolayer can thus be derived from the surface conductivity along each direction as [29]:

$$\varepsilon_{jj} = \varepsilon_r + \frac{i\sigma_{jj}}{\varepsilon_0 \omega d_B} \quad (2)$$

where $\epsilon_r = 11$ is the relative permittivity of borophene [29], ϵ_0 is the permittivity of free space, and d_B is the thickness of borophene. Similar to other 2D materials, the z -component permittivity of borophene is set as $\epsilon_{zz} = \epsilon_r$ [19,30].

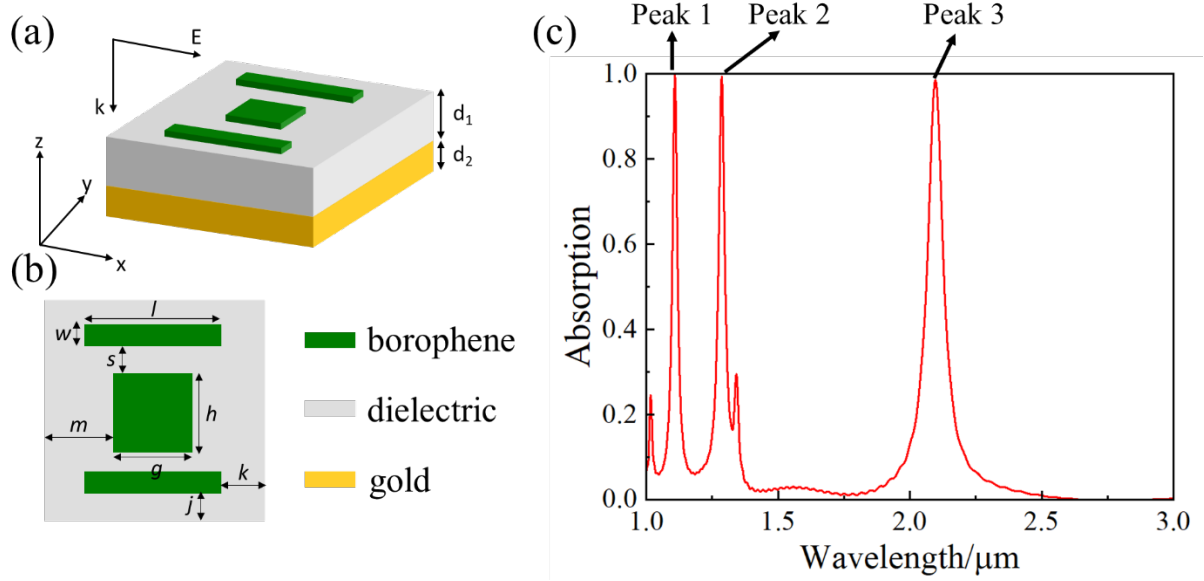


Fig. 1. (a) Global view and (b) top view of a unit cell in a typical borophene metadvice. (c) Absorption spectrum of a borophene metadvice under a normal incidence of light, when the geometric parameters of the patterned borophene layer are set as $l = 55$ nm, $w = 10$ nm, $g = 30$ nm, $h = 30$ nm, and $s = 20$ nm. The thicknesses of borophene, dielectric layer, and gold substrate are 0.3 nm, 150 nm and 100 nm, respectively.

Results and Discussion

Absorption peaks with high intensities are preferred to achieve excellent sensing performance for refractive index sensors [31]. The absorption spectra of the borophene metadvice under a normal incidence of light within the wavelength range of 1 to 3 μm are calculated. As shown in Fig. 1c, three nearly perfect absorption peaks located at $\lambda_1 = 1.108$ μm , $\lambda_2 = 1.286$ μm , and $\lambda_3 = 2.098$ μm , corresponding to absorptivities of 99.72%, 99.18%, and 98.13%, respectively, are obtained after optimizations of the geometric parameters ($l = 55$ nm, $w = 10$ nm, $g = 30$ nm, $h =$

30 nm, and $s = 20$ nm) of a typical borophene metadvice. Details of structural optimizations are shown in Supplementary Fig. S2.

To reveal the origin of the multi-peak absorption of the borophene metadvice, we further calculate the electric field distributions within the patterned borophene layer at the wavelengths of the absorption peaks (Fig. 2). At $\lambda_1 = 1.108 \mu\text{m}$, electric field enhancement $|E/E_0|$ primarily occurs at the edges of the nano-rectangle along the y axis (Fig. 2a). The z -component of the electric field (E_z) distribution shown in Fig. 2b indicates that strong E_z can be observed at the edges of the nano-rectangle along the y axis, along with weaker E_z distributed at the corners of the nano-rectangle. Apparent positive and negative dipoles are located at those positions (Supplementary Fig. S3), which can be attributed to the localized surface plasmon resonance effect [19,32] of the borophene nano-rectangle. Meanwhile, strong electric field localization can be observed in the R_1 region from the x -component of the electric field (E_x) distribution at λ_1 (Fig. 2c), indicating that the middle part of the borophene nano-rectangles provides principal channels for the energy transportation at λ_1 [19,33]. At $\lambda_2 = 1.286 \mu\text{m}$, electric field enhancement is mainly located at the four corners of the borophene nano-rectangle (Fig. 2d), which may arise from the corner effect due to the sharpness in shape [19]. The E_z distribution in Fig. 2e and Supplementary Fig. S3 shows that dipoles can also be observed at the four corners at λ_2 , with inverted ‘ \pm ’ signs compared to the ones at the four corners at λ_1 . Moreover, as shown in the E_x distribution in Fig. 2f, strong electric field localization in the R_2 region illustrates that the edges of the borophene nano-rectangle along x axis are the primary channels for the energy transportation at λ_2 . The results indicate that interactions between the borophene nano-rectangle and light lead to the formation of two strong absorption peaks at λ_1 and λ_2 . While at $\lambda_3 = 2.098 \mu\text{m}$, the electric field enhancement is mainly distributed along the edges of the borophene nano-ribbons (Fig. 2g). Detailed E_z distribution (Fig. 2h and Supplementary Fig.

S3) shows that positive and negative dipoles are observed at the edges of the nano-ribbons, and the x -component electric field is primarily located at the edges of the nano-ribbons (Fig. 2i), illustrating that plasmon hybridization between borophene nano-ribbons in adjacent unit cells along the x axis may have led to the formation of the absorption peak at λ_3 [32,34].

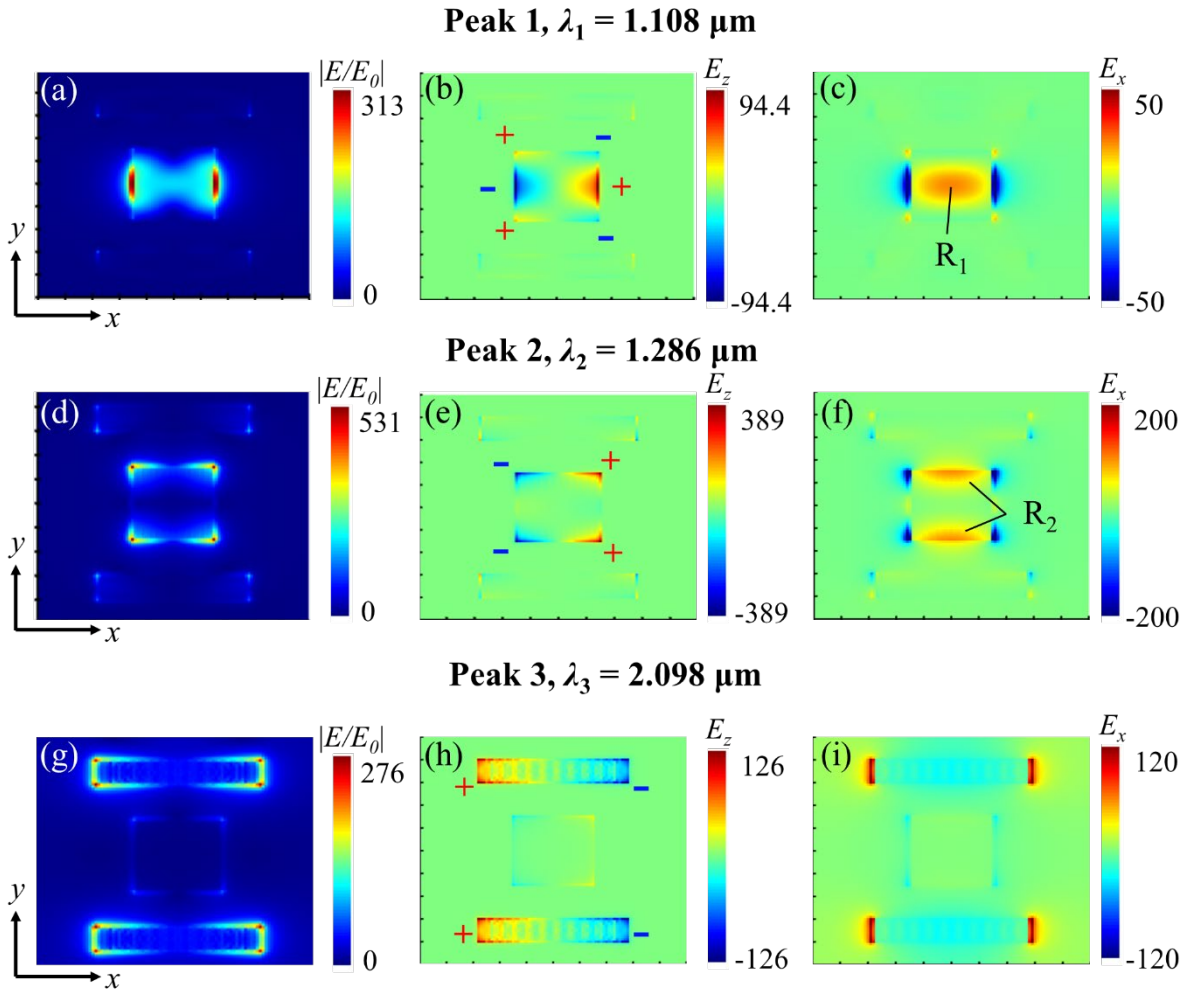


Fig. 2. Distributions of (a) the electric field enhancement $|E/E_0|$, (b) the z -component electric field E_z , and (c) the x -component electric field E_x within the patterned borophene layer in the x - y plane ($z = 350 \text{ nm}$) at the absorption peak $\lambda_1 = 1.108 \mu\text{m}$. Distributions of (d) the electric field enhancement $|E/E_0|$, (e) the z -component electric field E_z , and (f) the x -component electric field E_x within the patterned borophene layer in the x - y plane ($z = 350 \text{ nm}$) at the absorption peak $\lambda_2 = 1.286 \mu\text{m}$. Distributions of (g) the electric field enhancement $|E/E_0|$, (h) the z -component electric field E_z ,

and (i) the x -component electric field E_x within the patterned borophene layer in the x - y plane ($z = 350$ nm) at the absorption peak $\lambda_3 = 2.098$ μm .

Next, we demonstrate the outstanding refractive index sensing performance of the multi-peak borophene metadevices. Fig. 3a shows the absorption spectra of an optimized borophene metadevice ($l = 55$ nm, $w = 10$ nm, $g = 30$ nm, $h = 30$ nm, and $s = 20$ nm) under different environmental refractive indices (n_{env}). As n_{env} increases, all of the three resonant peaks shift to longer wavelengths. The sensitivity (S) of the refractive index sensor can thus be calculated by $S = \Delta\lambda/\Delta n_{env}$, where $\Delta\lambda$ represents the wavelength shift of the resonant peak, and Δn_{env} represents the change in the refractive index of the environment [9]. Figure of merit (FOM), indicating the optical resolution of the refractive index sensor [35], is calculated by $\text{FOM} = S/\text{FWHM}$, where FWHM represents the full width at half maximum of a resonance peak. Fig. 3b shows the resonant wavelengths of the peaks in the absorption spectra of the metadevice under different environmental refractive indices. The sensitivities at the three resonant wavelength peaks are calculated to be 339.1, 410.1, and 738.1 nm shift per refractive index units (nm/RIU), and the corresponding FOMs are calculated to be 15.41/RIU, 14.65/RIU and 10.85/RIU, respectively. Moreover, the normalized sensitivity S' is calculated to compare the performance of various sensors by: $S' = S/\lambda_{resonant}$, where $\lambda_{resonant}$ represents the resonant wavelength [9,31]. The calculated normalized sensitivities of the absorption peak1, peak 2 and peak 3 are 0.31/RIU, 0.32/RIU and 0.35/RIU, respectively, indicating the excellent sensing performance of the proposed multi-peak borophene refractive index sensors, comparable to or even higher than that of single-peak sensors reported in prior work (Supplementary Table S1).

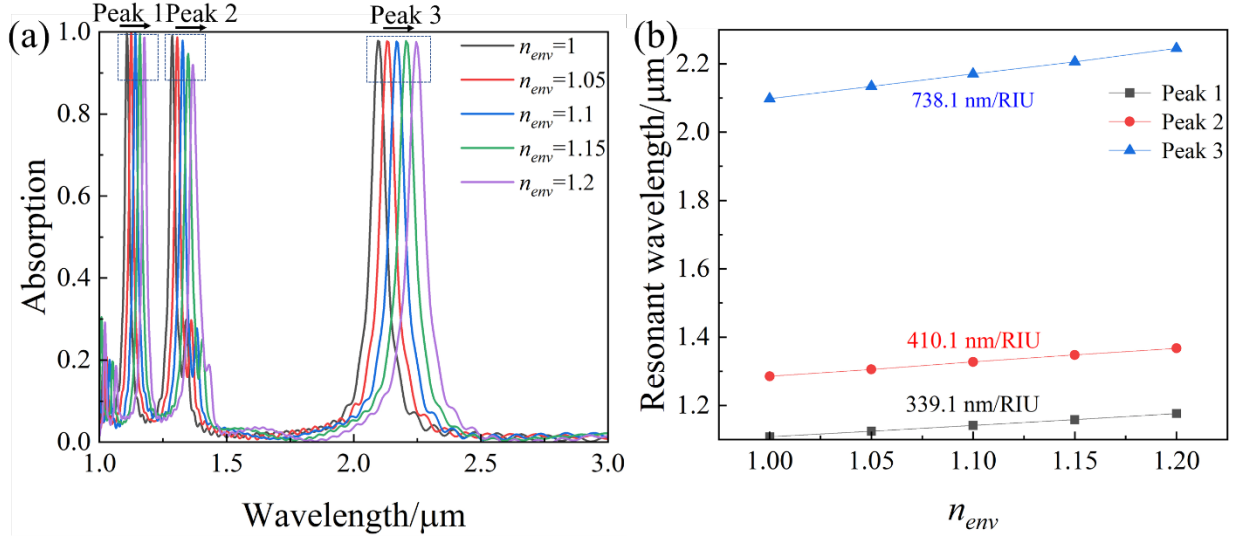


Fig. 3. (a) Absorption spectra of the borophene metadvice as the environmental refractive index n_{env} changes from 1 to 1.2. (b) Resonant wavelengths of the borophene metadvice under different n_{env} .

Compared to noble metals, the optical properties of borophene can be easily tuned by applying different external electric bias voltages to adjust the carrier density [14,36]. Fig. 4a shows the absorption spectra of the third absorption peak of the borophene sensors with different carrier densities (n_s) ranging from $3.3 \times 10^{19} \text{ m}^{-2}$ to $5.3 \times 10^{19} \text{ m}^{-2}$, while those of the first and the second peaks are shown in the Supplementary Fig. S4. When n_s increases, all the three absorption peaks are blue-shifted, and the *FWHM* of each peak narrows gradually. We further reveal the effect of n_s on the sensing performance of each absorption peak. As shown in Figs. 4b-d, the resonant wavelengths of the three absorption peaks versus n_{env} for the sensors with different n_s are plotted. When n_{env} increases, all the resonant peaks shift to longer wavelengths. Moreover, the sensitivity calculated at each resonant peak keeps increasing as n_s decreases, indicating the highly tunable properties of the borophene sensors. For instance, the sensitivity of the borophene metadvice

reaches up to 856.0 nm/RIU when the carrier density of borophene is adjusted to $3.3 \times 10^{19} \text{ m}^{-2}$ (Fig. 4d).

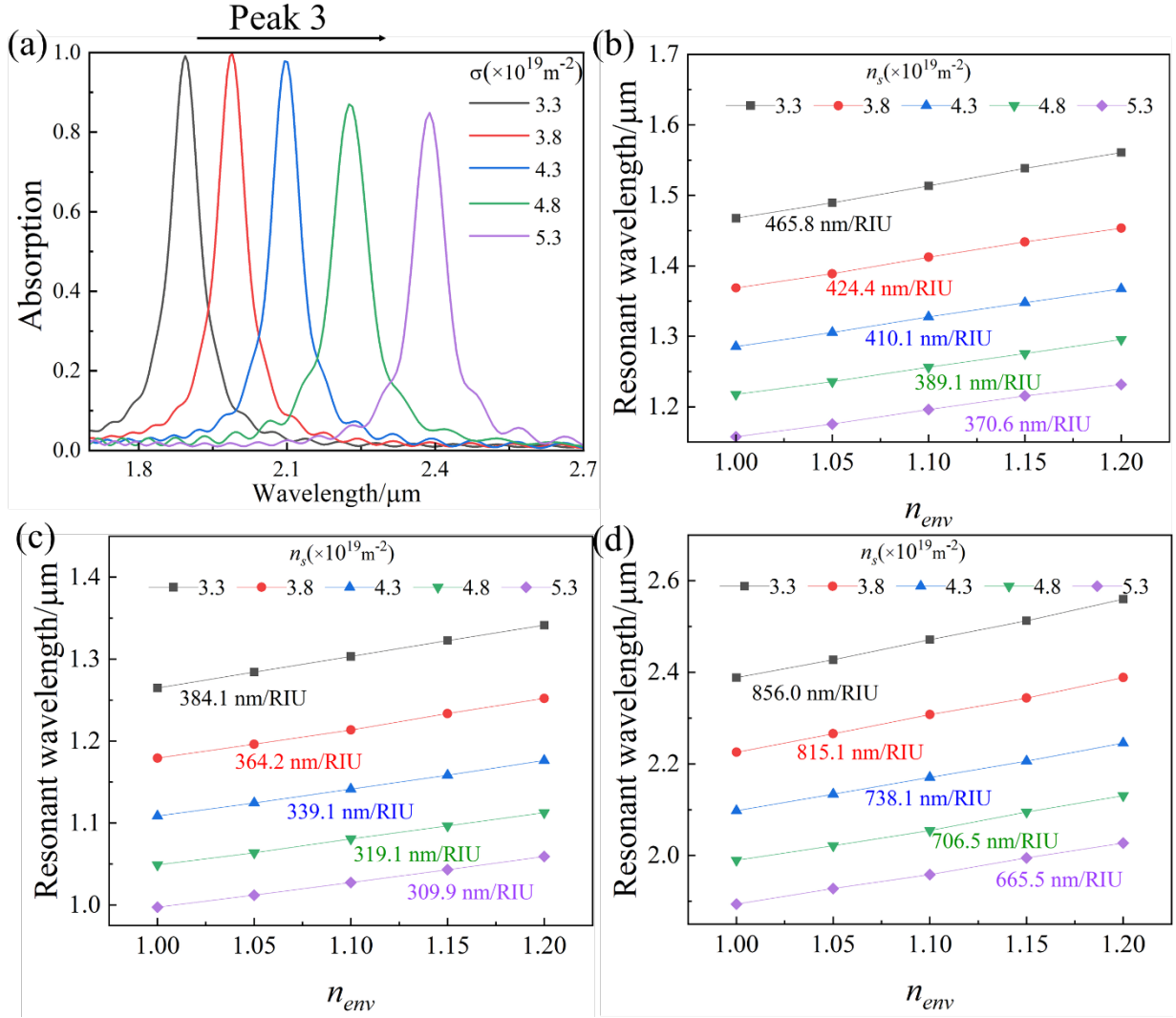


Fig. 4. (a) Absorption spectra of the third absorption peak of the borophene metadvice with different carrier densities (n_s) of borophene. (b) The resonant wavelengths of absorption peak 1 as functions of n_{env} under different n_s . (c) The resonant wavelengths of absorption peak 2 as functions of n_{env} under different n_s . (d) The resonant wavelengths of absorption peak 3 as functions of n_{env} under different n_s .

Conclusion

In summary, we have designed efficient borophene-based refractive index sensors with multiple nearly perfect absorption peaks in the near-IR regime. After optimizing the geometry parameters of the borophene metadevices, three strong absorption peaks with intensities of 99.72%, 99.18%, and 98.13% are achieved. Detailed analyses show that the sensitivities calculated at the peaks reach 339.1 nm/RIU, 410.1 nm/RIU, and 738.1 nm/RIU, and corresponding FOM reaches 15.41/RIU, 14.65/RIU and 10.85/RIU, respectively, exhibiting excellent sensing performance that is comparable to or even higher than that of single-peak refractive index sensors in prior work. In addition, we show that the working wavelength and sensing performance of the borophene sensors can be easily tuned by adjusting the carrier density of borophene. This study demonstrates the potential applications of borophene in the next-generation tunable sensing systems operating in the near-IR regime and provides useful insights into the design of multi-peak borophene-based optoelectronic and photonic nanodevices.

Funding information

The University of Texas at Dallas startup fund; National Science Foundation (Grant No. CBET-1937949).

Disclosures

The authors declare no conflicts of interest.

Data availability

The datasets analyzed during the current study are available from the corresponding author on reasonable request.

Supplemental document

See [Supplementary materials](#) for supporting content.

Reference

- [1] G.H. Silvestre, W.L. Scopel, R.H. Miwa, Electronic stripes and transport properties in borophene heterostructures, *Nanoscale*. 11 (2019) 17894–17903.
- [2] Y.V. Kaneti, D.P. Benu, X. Xu, B. Yulianto, Y. Yamauchi, D. Golberg, Borophene: Two-dimensional Boron Monolayer: Synthesis, Properties, and Potential Applications, *Chemical Reviews*. (2021).
- [3] G. Sachdeva, S. Kaur, R. Pandey, S.P. Karna, First-Principles Study of Linear and Nonlinear Optical Properties of Multi-Layered Borophene, *Computation*. 9 (2021) 101.
- [4] T. Abasi, A. Boochani, R. Masharian, The Electronic and Optical Properties of 2D Boron Sheet with cmmm Space Group, *Journal of Research on Many-Body Systems*. 11 (2021) 1–13.
- [5] P. Bhatt, K. Kaur, J. George, Enhanced Charge Transport in Two-Dimensional Materials through Light–Matter Strong Coupling, *ACS Nano*. 15 (2021) 13616–13622.
- [6] Y. Li, Y. Chen, H. Zhou, H. Zhu, Transient Optical Modulation of Two-Dimensional Materials by Excitons at Ultimate Proximity, *ACS Nano*. 15 (2021) 5495–5501.
- [7] N. Rohaizad, C.C. Mayorga-Martinez, M. Fojtů, N.M. Latiff, M. Pumera, Two-dimensional materials in biomedical, biosensing and sensing applications, *Chemical Society Reviews*. 50 (2021) 619–657.
- [8] Z. He, L. Li, H. Ma, L. Pu, H. Xu, Z. Yi, X. Cao, W. Cui, Graphene-based metasurface sensing applications in terahertz band, *Results in Physics*. 21 (2021) 103795. <https://doi.org/10.1016/j.rinp.2020.103795>.
- [9] J. Zhang, Z. Zhang, X. Song, H. Zhang, J. Yang, Infrared plasmonic sensing with anisotropic two-dimensional material borophene, *Nanomaterials*. 11 (2021) 1165.
- [10] F. Xia, H. Wang, D. Xiao, M. Dubey, A. Ramasubramaniam, Two-dimensional material nanophotonics, *Nature Photonics*. 8 (2014) 899–907.
- [11] M. Pan, H. Huang, B. Fan, W. Chen, S. Li, Q. Xie, F. Xu, D. Wei, J. Fang, Theoretical design of a triple-band perfect metamaterial absorber based on graphene with wide-angle insensitivity, *Results in Physics*. 23 (2021) 104037.
- [12] R. Li, Y. Zheng, Y. Luo, J. Zhang, Z. Yi, L. Liu, Q. Song, P. Wu, Y. Yu, J. Zhang, Multi-peak narrow-band perfect absorber based on two-dimensional graphene array, *Diamond and Related Materials*. 120 (2021) 108666.
- [13] Y. Huang, S.N. Shirodkar, B.I. Yakobson, Two-dimensional boron polymorphs for visible range plasmonics: a first-principles exploration, *Journal of the American Chemical Society*. 139 (2017) 17181–17185.
- [14] S.A. Dereshgi, Z. Liu, K. Aydin, Anisotropic localized surface plasmons in borophene, *Optics Express*. 28 (2020) 16725–16739.
- [15] T.A. Morgado, M.G. Silveirinha, Active graphene plasmonics with a drift-current bias, *ACS Photonics*. 8 (2021) 1129–1136.
- [16] L. Cui, M. Sun, Graphene Plasmon-Enhanced Polarization-Dependent Interfacial Charge Transfer Excitons in 2D Graphene-Black Phosphorus Heterostructures in NIR and MIR Regions, *The Journal of Physical Chemistry C*. 125 (2021) 22370–22378.
- [17] H. Xia, C. Wang, S. Blais, J. Yao, Ultrafast and precise interrogation of fiber Bragg grating sensor based on wavelength-to-time mapping incorporating higher order dispersion, *Journal of Lightwave Technology*. 28 (2010) 254–261.

- [18] M.B. Ross, M.G. Blaber, G.C. Schatz, Using nanoscale and mesoscale anisotropy to engineer the optical response of three-dimensional plasmonic metamaterials, *Nature Communications*. 5 (2014) 1–11.
- [19] R. Zhou, J. Peng, S. Yang, D. Liu, Y. Xiao, G. Cao, Lifetime and nonlinearity of modulated surface plasmon for black phosphorus sensing application, *Nanoscale*. 10 (2018) 18878–18891. <https://doi.org/10.1039/C8NR06796A>.
- [20] C. Lian, S.-Q. Hu, J. Zhang, C. Cheng, Z. Yuan, S. Gao, S. Meng, Integrated plasmonics: Broadband dirac plasmons in borophene, *Physical Review Letters*. 125 (2020) 116802.
- [21] B. Zhao, J.-H. Song, M. Brongersma, S. Fan, Atomic-scale control of coherent thermal radiation, *ACS Photonics*. 8 (2021) 872–878.
- [22] D.U. Yildirim, A. Ghobadi, M.C. Soydan, M. Gokbayrak, A. Toprak, B. Butun, E. Ozbay, Colorimetric and near-absolute polarization-insensitive refractive-index sensing in all-dielectric guided-mode resonance based metasurface, *The Journal of Physical Chemistry C*. 123 (2019) 19125–19134.
- [23] A.J. Ollanik, I.O. Oguntoye, G.Z. Hartfield, M.D. Escarra, Highly Sensitive, Affordable, and Adaptable Refractive Index Sensing with Silicon-Based Dielectric Metasurfaces, *Advanced Materials Technologies*. 4 (2019) 1800567.
- [24] G.-Y. Yao, Q.-L. Liu, Z.-Y. Zhao, Studied localized surface plasmon resonance effects of Au nanoparticles on TiO₂ by FDTD simulations, *Catalysts*. 8 (2018) 236.
- [25] Y. Fang, K. Wen, Y. Qin, Z. Li, B. Wu, Multiple fano resonances in an end-coupled MIM waveguide system, *Optics Communications*. 452 (2019) 12–17.
- [26] H. Durmaz, Y. Li, A.E. Cetin, A multiple-band perfect absorber for SEIRA applications, *Sensors and Actuators B: Chemical*. 275 (2018) 174–179. <https://doi.org/10.1016/j.snb.2018.08.053>.
- [27] B. Zhao, Z.M. Zhang, Strong plasmonic coupling between graphene ribbon array and metal gratings, *Acs Photonics*. 2 (2015) 1611–1618.
- [28] W.M. Haynes, *CRC handbook of chemistry and physics*, CRC press, 2014.
- [29] T. Liu, C. Zhou, S. Xiao, Tailoring anisotropic absorption in a borophene-based structure via critical coupling, *Optics Express*. 29 (2021) 8941–8950.
- [30] S. Asgari, N. Granpayeh, Tunable mid-infrared refractive index sensor composed of asymmetric double graphene layers, *IEEE Sensors Journal*. 19 (2019) 5686–5691.
- [31] S. Wu, R. Jian, G. Xiong, High-performance polarization-independent black phosphorus refractive index sensors enabled by a single-layer pattern design, *Optics Letters*. 47 (2022) 517–520.
- [32] Y. Zhu, B. Tang, C. Jiang, Tunable ultra-broadband anisotropic absorbers based on multi-layer black phosphorus ribbons, *Applied Physics Express*. 12 (2019) 032009.
- [33] D. Liu, L. Wu, Q. Liu, R. Zhou, S. Xie, J. Chen, M. Wu, L. Zeng, Plasmon switching effect based on graphene nanoribbon pair arrays, *Optics Communications*. 377 (2016) 74–82.
- [34] Z. Liu, K. Aydin, Localized surface plasmons in nanostructured monolayer black phosphorus, *Nano Letters*. 16 (2016) 3457–3462.
- [35] R. Ameling, L. Langguth, M. Hentschel, M. Mesch, P.V. Braun, H. Giessen, Cavity-enhanced localized plasmon resonance sensing, *Applied Physics Letters*. 97 (2010) 253116.
- [36] A. Farmani, Three-dimensional FDTD analysis of a nanostructured plasmonic sensor in the near-infrared range, *JOSA B*. 36 (2019) 401–407.